

Flexible silicon solar cells with high power-to-weight ratios

<https://doi.org/10.1038/s41586-023-06948-y>

Received: 24 October 2022

Accepted: 6 December 2023

Published online: 31 January 2024

 Check for updates

Yang Li^{1,2,3,5}, Xiaoning Ru^{2,5}, Miao Yang^{2,5}, Yuhe Zheng^{1,5}, Shi Yin², Chengjian Hong², Fuguo Peng², Minghao Qu², Chaowei Xue², Junxiong Lu², Liang Fang², Chao Su¹, Daifen Chen¹, Junhua Xu³, Chao Yan³, Zhenguo Li², Xixiang Xu² & Zongping Shao⁴

Silicon solar cells are a mainstay of commercialized photovoltaics, and further improving the power conversion efficiency of large-area and flexible cells remains an important research objective^{1,2}. Here we report a combined approach to improving the power conversion efficiency of silicon heterojunction solar cells, while at the same time rendering them flexible. We use low-damage continuous-plasma chemical vapour deposition to prevent epitaxy, self-restoring nanocrystalline sowing and vertical growth to develop doped contacts, and contact-free laser transfer printing to deposit low-shading grid lines. High-performance cells of various thicknesses (55–130 μm) are fabricated, with certified efficiencies of 26.06% (57 μm), 26.19% (74 μm), 26.50% (84 μm), 26.56% (106 μm) and 26.81% (125 μm). The wafer thinning not only lowers the weight and cost, but also facilitates the charge migration and separation. It is found that the 57- μm flexible and thin solar cell shows the highest power-to-weight ratio (1.9 W g^{-1}) and open-circuit voltage (761 mV) compared to the thick ones. All of the solar cells characterized have an area of 274.4 cm^2 , and the cell components ensure reliability in potential-induced degradation and light-induced degradation ageing tests. This technological progress provides a practical basis for the commercialization of flexible, lightweight, low-cost and highly efficient solar cells, and the ability to bend or roll up crystalline silicon solar cells for travel is anticipated.

Crystalline silicon (c-Si) solar cells have been the mainstay of green and renewable energy³, accounting for 3.6% of global electricity generation and becoming the most cost-effective option for new electricity generation in most of the world⁴. Although c-Si solar cells now account for more than 95% of the market for solar cells, which usually have a wafer thickness of 150–180 μm , their use is infeasible in some extreme application scenarios, such as satellites, spacecraft and unmanned aerial vehicles, and there is a need for further weight reduction and flexibility of solar cells⁵. Thus, reducing the thickness of the c-Si wafer to much thinner than that in typical c-Si solar cells, and thereby incorporating the advantages of ‘thin-film solar cells’ into c-Si solar cells, is the focus of much research^{1,6,7}. However, the power conversion efficiencies (PCEs) of all of the thin c-Si solar cells (55–130 μm) studied have remained in the range of 23.27–24.70% for decades^{8–13}.

Recently, front-back contact silicon heterojunction (SHJ) solar cells have become a formidable contender for the next generation of photovoltaic devices owing to their advantages in double-sided power generation, low cost and scalable production, compared to the interdigitated back contact configurations¹⁴. To further improve the performance of front-back contact SHJ solar cells on the premise of bendable thicknesses (<130 μm), careful research and optimization

of each technical step (passivation, doped contact layer growth, metal oxide conductive layer deposition and grid line printing), as well as effectively connecting all of the steps while avoiding unnecessary damage to the interfaces, are essential.

Highly efficient flexible and thin SHJ solar cells

On the basis of our research, c-Si solar cells of >26% PCE with thicknesses in the range of 55–130 μm , possessing features of both high PCE and flexibility, can be produced. Therefore, flexibility must be taken into consideration as an important factor. We divided the c-Si solar cells into categories according to the minimum bending radius of curvature (r_b): nonflexible cells ($r_b > 63 \text{ mm}$) with thicknesses of >150 μm ; semiflexible (SF) cells ($38 \text{ mm} < r_b < 63 \text{ mm}$) with thicknesses of between 100 and 150 μm ; and flexible and thin (FT) cells ($r_b < 38 \text{ mm}$) with thicknesses of <100 μm (thinner than a piece of A4 paper). Thus, we demonstrate the potential of c-Si solar cells to become a category of thin-film solar cells with remarkable flexibility and plasticity (Fig. 1a), the cells can undergo various deformations, such as bending and curling. By contrast, traditional c-Si solar cells ($\geq 150 \mu\text{m}$) immediately break with a relatively small distortion.

¹School of Energy and Power, Jiangsu University of Science and Technology, Zhenjiang, Jiangsu, China. ²LONGi Central R&D Institute, LONGi Green Energy Technology Co., Ltd, Xi'an, Shaanxi, China. ³School of Materials Science and Engineering, Jiangsu University of Science and Technology, Zhenjiang, Jiangsu, China. ⁴WA School of Mines: Minerals, Energy and Chemical Engineering (WASM-MECE), Curtin University, Perth, Western Australia, Australia. ⁵These authors contributed equally: Yang Li, Xiaoning Ru, Miao Yang, Yuhe Zheng. ✉e-mail: dfchen@just.edu.cn; jhxu@just.edu.cn; chaoyan@just.edu.cn; lzg@longi.com; xuxixiang@longi.com; zongping.shao@curtin.edu.au

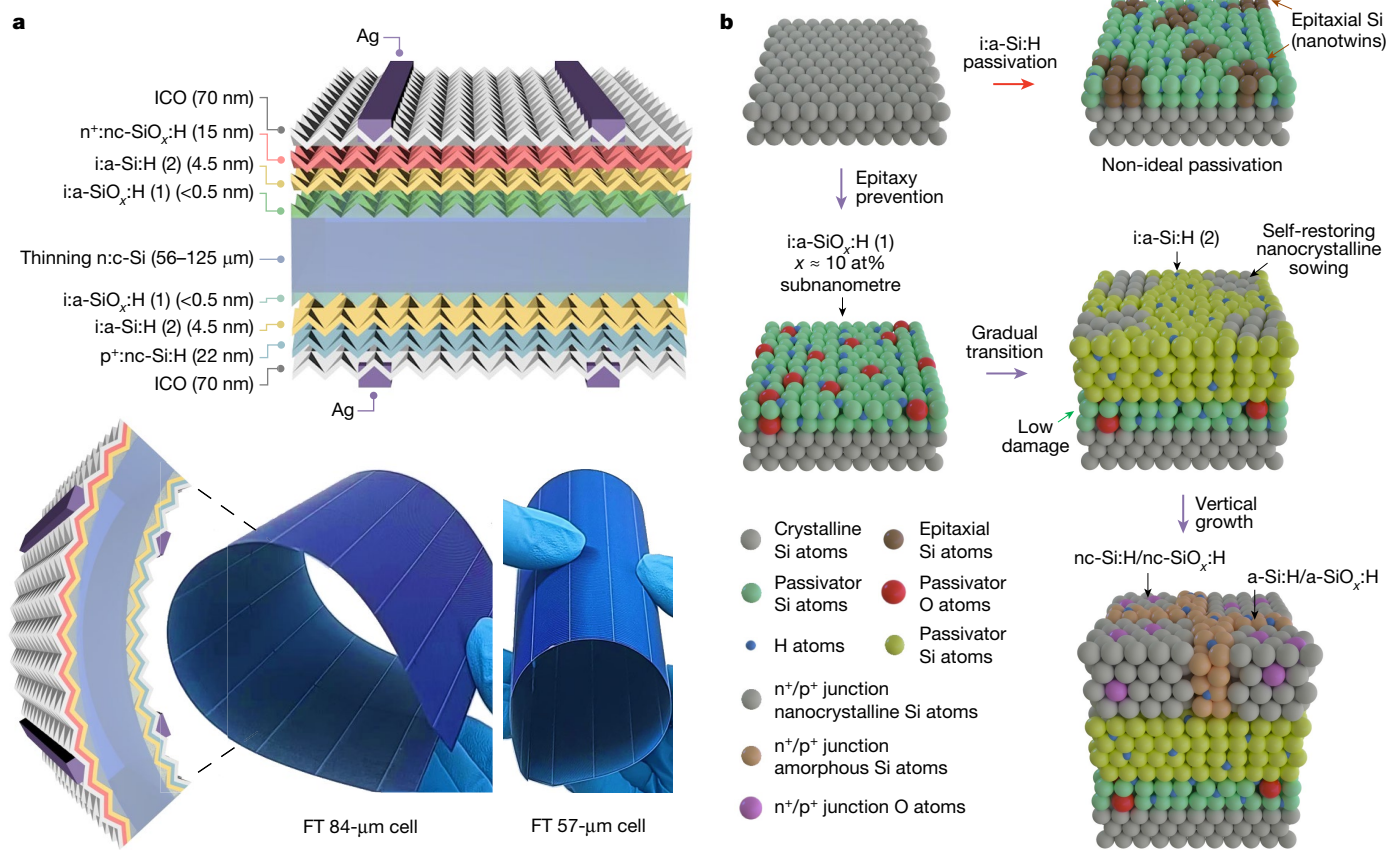


Fig. 1 | Schematic diagrams of the FT and SF SHJ solar cells. **a**, Structure schematics and photographs of the FT and SF SHJ solar cells (166 × 166 mm). **b**, Schematic diagrams of the continuous-plasma CVD composite gradient passivation, the nanocrystalline sowing and the vertical growth induction steps. During continuous-plasma CVD, the RF plasma is kept stable

Epitaxy-preventing composite gradient passivation

The first step in resolving the efficiency bottleneck of FT and SF cells is to achieve good passivating contacts. For SHJ solar cells, passivation is typically implemented using intrinsic hydrogenated amorphous silicon ($i\text{:a-Si:H}$) or hydrogen-rich $i\text{:a-Si:H}$ passivation layers in conventional techniques^{15–18}, but epitaxial dendrite growth from the c-Si surface is inevitable (Extended Data Fig. 1a,b). Although oxygen doping is considered to be beneficial in suppressing epitaxial growth, it is associated with a decrease in the electrical properties of the passivating contacts¹⁹. In this work, a two-stage composite gradient passivation process was adopted to resolve this contradiction (Fig. 1b). In the first stage, 2–3 atomic layers of an oxygen-containing amorphous silicon subnanolayer (<0.5 nm; $i\text{:a-SiO}_x\text{:H}$ (1) $x \approx 10$ at%) were bifacially grown on c-Si by plasma-enhanced chemical vapour deposition (PECVD). The ultrathin passivation layer $i\text{:a-SiO}_x\text{:H}$ (1) prevents the periodicity of the crystal arrangement of c-Si from continuing outwards, while minimizing the impact of oxygen doping on the electrical properties of the passivation contacts. In the second stage, an epitaxy-free $i\text{:a-Si:H}$ (2) passivation layer with a thickness of about 4.5 nm was intentionally coated on $i\text{:a-SiO}_x\text{:H}$ (1) to strengthen the passivation effect and isolate the subsequent doping layers. The enlarged cross-sectional morphology in Extended Data Fig. 1c highlights the various regions of the composite gradient passivation layers and demonstrates that the ultrathin oxygen-doped subnanolayer fundamentally prevented the formation of epitaxial silicon nanotwins. Compared with the traditional hydrogen-rich $i\text{:a-Si:H}/a\text{-Si:H}$, the

(fluctuation $\pm 0.5\%$) under the real-time monitoring and rapid-response regulation without reignition to protect the epitaxy-preventing $i\text{:a-SiO}_x\text{:H}$ (1) subnanolayer. During the composite gradient passivation, the low-damage $i\text{:a-SiO}_x\text{:H}$ (1)/ $a\text{-Si:H}$ (2) composite passivation layers with a gradual transitional interface are created through the continuous-plasma CVD process.

$i\text{:a-SiO}_x\text{:H}$ (1)/ $a\text{-Si:H}$ (2) composite passivation layers increased the PCE by 0.34% (Fig. 2a).

Low-damage continuous-plasma CVD operation

We realized that the conventional discontinuous-plasma CVD process is not ideal, as the subnanolayer is vulnerable and highly sensitive to the plasma fluctuation and reignition (transient high-voltage surges). After being subjected to the stepwise PECVD procedure, $i\text{:a-SiO}_x\text{:H}$ (1) was found to have perforating defects distributed on its surface, and the peak roughness was 0.5 nm (Fig. 2b). These devastating vacancies can serve as a new foundation for c-Si epitaxial growth, impairing the passivation function of $i\text{:a-SiO}_x\text{:H}$ (1). Hence, we adjusted the commonly used step-by-step procedure to a one-step continuous-plasma CVD passivation process, so that $i\text{:a-Si:H}$ (2) can be continuously grown on $i\text{:a-SiO}_x\text{:H}$ (1) while guaranteeing the integrity of the epitaxy-preventing $i\text{:a-SiO}_x\text{:H}$ (1) subnanolayer (Fig. 2c) and the optimal passivation effect can be obtained. Notably, the continuous process produced a naturally evolving rather than abrupt interface between the $i\text{:a-SiO}_x\text{:H}$ (1)/ $a\text{-Si:H}$ (2) composite passivation layers (Extended Data Fig. 1c), because of the gradual transition of the feed gases. The hydrogen content (C_H) and microstructure factor (R') are two key parameters influencing the passivation quality, which need to be individualized in $i\text{:a-SiO}_x\text{:H}$ (1) and $i\text{:a-Si:H}$ (2) owing to their differentiated functions. High C_H is required for $i\text{:a-SiO}_x\text{:H}$ (1) to saturate dangling bonds, whereas tailoring C_H for $i\text{:a-Si:H}$ (2) focuses more on boosting the output. As a result, we can see from Fig. 2d that the effective minority carrier lifetime (τ_{eff}) climbed to

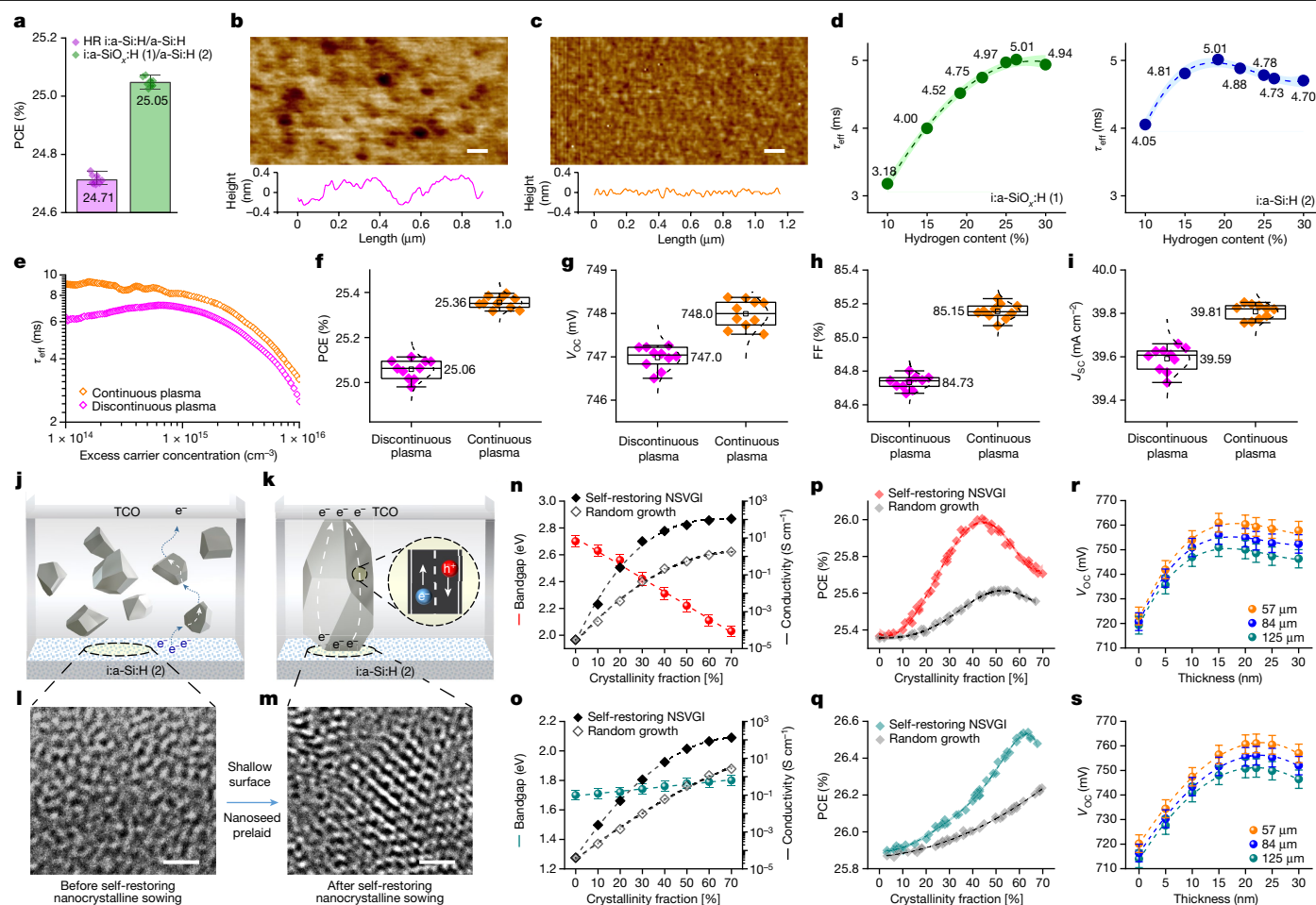


Fig. 2 | Passivation and nanocrystalline contacts. **a**, Gain effect of $i\text{:a-SiO}_x\text{:H (1)}/\text{a-Si:H (2)}$ on the cell performance (HR, hydrogen rich). **b, c**, Atomic force micrographs (top) and the corresponding surface profiles (bottom) of $i\text{:a-SiO}_x\text{:H (1)}$ after the discontinuous-plasma (**b**) and continuous-plasma (**c**) CVD processes. Scale bars, 100 nm. **d**, Variation of the effective minority carrier lifetime (τ_{eff}) with hydrogen content in the composite passivation layers (continuous plasma). **e**, Enhanced τ_{eff} through the continuous-plasma CVD passivation approach (excess carrier density of $5 \times 10^{15} \text{ cm}^{-3}$). **f–i**, Improved cell performance through the continuous-plasma CVD passivation approach. **j**, Schematic of the traditional nanocrystallization approach. **k**, Schematic of the self-restoring nanocrystalline sowing and vertical growth induction

process. **l, m**, HRTEM images of the passivation layer surface before and after the self-restoring nanocrystalline sowing. Scale bars, 1 nm. **n**, Variation of the bandgap and conductivity of the $n^+:\text{nc-SiO}_x\text{:H}$ window layer with crystallinity fraction. **o**, Variation of the bandgap and conductivity of the $p^+:\text{nc-Si:H}$ rear emitter with crystallinity fraction. **p**, Relationship between the PCE and crystallinity fraction of the $n^+:\text{nc-SiO}_x\text{:H}$ window layer with a $p^+:\text{a-Si:H}$ rear emitter. **q**, Relationship between the PCE and crystallinity fraction of the $p^+:\text{nc-Si:H}$ rear emitter with the optimal $n^+:\text{nc-SiO}_x\text{:H}$ window layer. **r**, V_{oc} curves with different thicknesses of the $n^+:\text{nc-SiO}_x\text{:H}$ window layer. **s**, V_{oc} curves with different thicknesses of the $p^+:\text{nc-Si:H}$ rear junction. The dashed lines in **d, n–s** are fit lines to evaluate the trends in the data.

the maximum value (about 5 ms) as C_{H} increased to 26.3% (R^* 68.9%) and 19.2% (R^* 20.2%) for $i\text{:a-SiO}_x\text{:H (1)}$ and $i\text{:a-Si:H (2)}$, respectively, which was also a notable improvement over that of the conventional passivation strategies (Extended Data Table 1a). In terms of cell performance, the open-circuit voltage (V_{oc}), fill factor (FF) and PCE all experienced the greatest gains under the optimal passivation conditions (Extended Data Fig. 2). By contrast, under the same conditions, τ_{eff} was reduced to 4.4 ms through the discontinuous-plasma CVD passivation operation (Fig. 2e), indicating degradation of the passivation effect and cell performance. On the basis of the above optimization, the cell performance is clearly comprehensively improved through protective continuous-plasma CVD, and the average values of PCE, FF, V_{oc} and the short-circuit current (J_{sc}) can be further increased by 0.30%, 0.42%, 1.0 mV and 0.22 mA cm^{-2} , respectively, compared with those of the discrete PECVD process (Fig. 2f–i).

Nanocrystalline sowing and contact vertical growth

Then n - and p -type carrier-selective contacts were grown by very high-frequency (VHF)-PECVD on the passivation layers, playing the

roles of the electron transport layer (ETL) and hole transport layer (HTL), respectively. According to the schematic in Fig. 2j, in traditional nanocrystallization routes, the nanocrystals are randomly dispersed in the contact layers and not coherent in the longitudinal direction, clearly visible in the high-resolution transmission electron microscopy (HRTEM) image in Extended Data Fig. 3a, which impedes the carrier separation and extraction efficiency^{20–23}. Instead, we used a self-restoring nanocrystalline sowing technique to induce vertical growth of doping junctions on both sides, as depicted in Fig. 1b, further reducing the electrical resistive loss and parasitic absorption loss in the direction of current flow (Fig. 2k). We discovered that using VHF CO_2 plasma to treat the $i\text{:a-Si:H (2)}$ surface can dehydrogenate it and encourage a transformation of the original amorphous state (Fig. 2l) to a partially nanocrystallized (nc-) state, and the nanoscale crystalline seeds can be observed after the prerequisite incubation (Fig. 2m). However, the trade-off is that the crystallization process is unrestricted, causing unwanted C_{H} loss in the bulk passivation layers as a function sowing duration (Extended Data Fig. 4c, d), and the cross-sectional HRTEM image (Extended Data Fig. 4e) testifies that if not controlled, reverse epitaxy would occur,

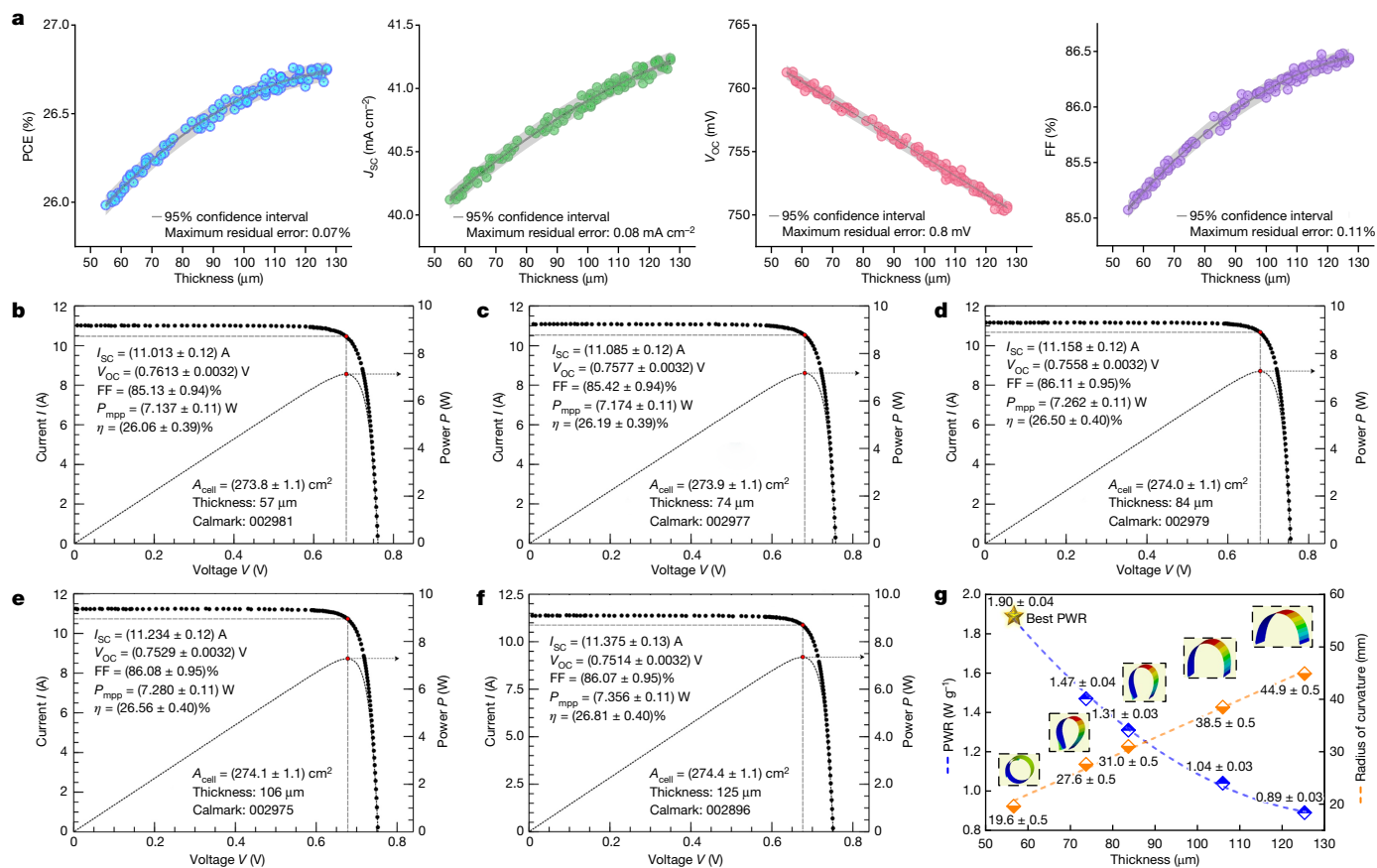


Fig. 3 | Parameter statistics and certification reports. **a**, Statistical parameters of 100 cells with various thicknesses. **b–f**, Institute for Solar Energy Research in Hamelin-certified current–voltage (I - V) and power–voltage (P - V) curves of the FT and SF SHJ solar cells with thicknesses of 57 μm (**b**), 74 μm (**c**),

84 μm (**d**), 106 μm (**e**) and 125 μm (**f**). mpp, maximum power point. **g**, PWR data and flexibility of the FT and SF SHJ solar cells. The dashed lines are fit lines to evaluate the trends in the data.

as the nanocrystals extend from the surface nanoseeds to the interior of i :a-Si:H (2), resulting in degradation of the passivation quality. As a result, we implemented a new self-restoring nanocrystalline sowing technology by introducing an effectively coordinated two-component VHF plasma of H_2 and CO_2 . The hydrogen atoms in the bifunctional plasma can spontaneously diffuse inside to restore C_H (Extended Data Fig. 4c,d) while restricting the nanocrystalline sowing on the shallow surface of i :a-Si:H (2). Subsequently, the doped contact layers germinated and grew upwards from the pre-laid nanoseeds, opening up ‘photogenerated carrier superhighways’ between the upper and lower layers, and the corresponding cross-sectional HRTEM image is shown in Extended Data Fig. 3b. Ultimately, with the assistance of the self-restoring nanocrystalline sowing and vertical growth induction process, the carrier conductivities of the contact layers exponentially increased with the crystallinity fraction (X_c), from 10^{-5} S cm^{-1} in the state with a low nanocrystalline fraction to $>10^2$ S cm^{-1} in the state with a high nanocrystalline fraction (Fig. 2n,o), approximately 1–2 orders of magnitude higher than those in traditional nanocrystallization routes. However, there is a trade-off for the selection of the X_c values. For the front n^+ :nc-SiO_x:H window layer, the increasing X_c hampers the formation of strong Si–O bonds (8.4 eV), narrowing the bandgap (Fig. 2n) and limiting the incident light transmittance. Therefore, the X_c of n^+ :nc-SiO_x:H was optimized to 43.7% when the PCE was taken into account (Fig. 2p), and the FF showed a similar trend with X_c (Extended Data Fig. 4a). By contrast, the rear junction (p^+ :nc-Si:H) can withstand a higher crystallinity to facilitate the hole transport because the impact of incident light does not need to be accounted for. Nevertheless, a high X_c hinders the boron-dopant subbands from incorporating the intrinsic

band structure, which causes a rapid increase in the bandgap of the HTL and increases the transparency for the longwave transmission (Fig. 2o). Simultaneously, the moderate X_c is advantageous for shortening the growth duration and maintaining the crystal coherence. Therefore, the cell performance peaked at a rear emitter crystallinity of 63.4% (Fig. 2q and Extended Data Fig. 4b). By comparison, the effects of the traditional nanocrystalline routes were much less, as shown in grey in Fig. 2p,q. In addition, the ETL and HTL layers require certain thicknesses to generate sufficient depletion regions for carrier separation, but excess thicknesses can result in same-polarity repelling and carrier recombination. As the window layer, the n^+ :nc-SiO_x:H ETL needs to be thinner to allow the maximum number of photons to be incident into the active layer. Therefore, after compromising the above three conditions, the thicknesses of the n^+ :nc-SiO_x:H ETL and the p^+ :nc-Si:H HTL were optimized to 15 nm and 22 nm, respectively, at which the V_{oc} curves reached the maxima, indicating the optimal electron and hole separation effect (Fig. 2r,s).

Ce-doped indium oxide and laser transfer printing

The passivating contacts are nondegenerate semiconductors exhibiting low lateral conductivity, so highly degenerate transparent conducting oxide (TCO) layers are stacked on silicon contacts to assist in collecting carriers to electrodes. Cerium-doped indium oxide (ICO) has been attracting increasing interest for solar cell applications owing to its excellent mobility and transparency^{24,25}. In a typical sputtering process for TCO layer deposition, the plasma ions directly bombard the sample surface, resulting in degradation of the cell performance.

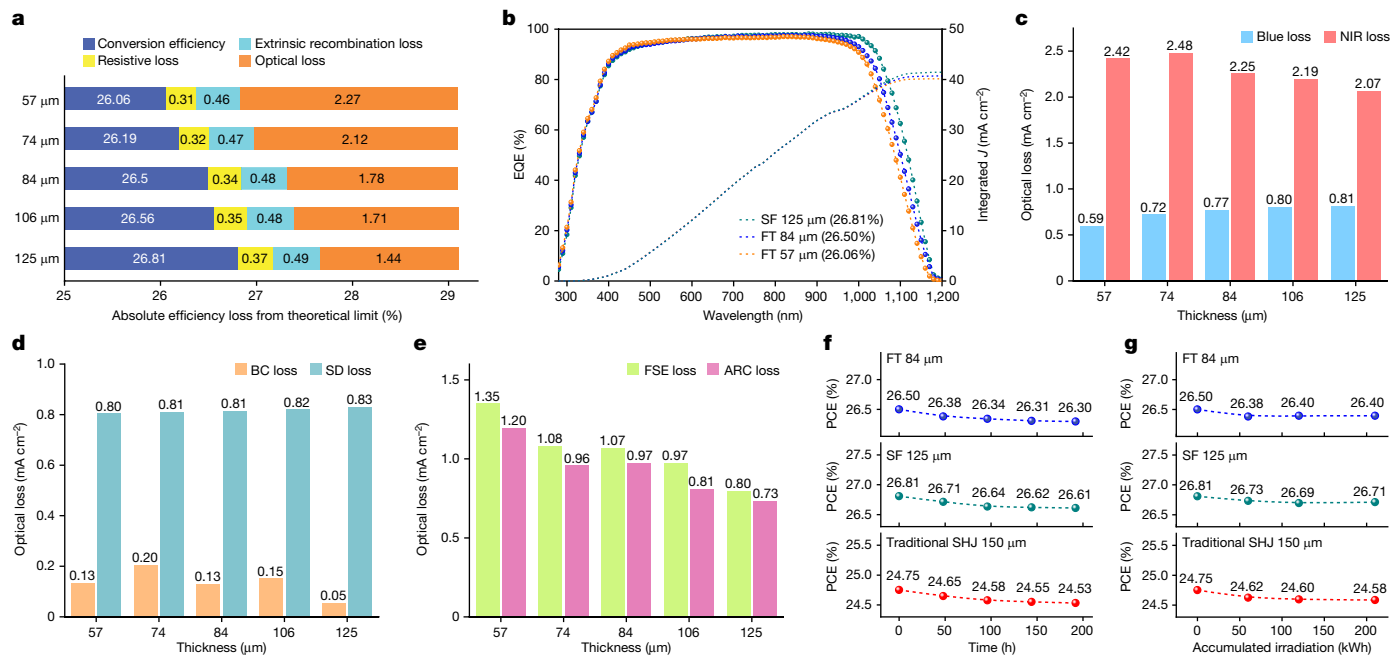


Fig. 4 | Quantum efficiencies, loss elements and stabilities. **a**, Summary of loss elements for the FT and SF SHJ solar cells relative to the practical limit (29.1%). **b**, External quantum efficiency (EQE) of the FT (57 and 84 μm) and SF (125 μm) solar cells. **c**, NIR and blue optical losses of the FT and SF solar cells. **d**, Shading (SD) and base collection (BC) losses of the FT and SF solar cells.

e, Antireflection coating (ARC) and front surface escape (FSE) losses of the FT and SF solar cells. **f**, Certificated PID ageing tests. **g**, Certificated light-induced degradation ageing tests. The dashed lines in **f, g** are fit lines to evaluate the trends in the data.

In this work, we deposited ICO as the TCO coating by the low-damage reactive plasma deposition method, which produced superior electrical performance, including much lower resistivity ($2.7 \times 10^{-4} \Omega \text{ cm}$) and higher carrier mobility ($83.1 \text{ cm V}^{-1} \text{ s}^{-1}$), when compared to those of the magnetron sputtering-derived indium tin oxide (Extended Data Table 1b) and other TCOs reported elsewhere²⁶. The TCO innovation not only contributed a 0.1% reduction in the total electrical power loss, but also played a decisive role in subsequent stability improvement. Afterwards, we strived to reduce optical loss by optimizing the configuration of grid lines using industry-compatible contact-free laser transfer printing (LTP) technology²⁷. The finger width could be reduced from 40 μm (typical screen printing) to 18 μm , with the shading area controlled to less than 2%. Extended Data Fig. 5 verifies that LTP makes a great contribution to J_{sc} and the PCE, increasing them by 0.33 mA cm^{-2} and 0.22%, respectively.

Cell performance and certification

Since Sanyo suggested wafer thinning as a strategy to maximize economic benefits, researchers have been exploring ways to improve the performance of thin-wafer c-Si solar cells¹²; however, it remains a great challenge to break through the 26% barrier for SF, and especially FT, solar cells^{8,13,28}. Through investigation of the above mechanism and technical innovation, we were able to achieve efficiencies above 26% in the full range of 55–130 μm , as shown in Fig. 3a, and certified by the Institute for Solar Energy Research in Hamelin. The certificates for the cells with thicknesses of 57 μm (26.06%), 74 μm (26.19%), 84 μm (26.50%), 106 μm (26.56%) and 125 μm (26.81%) are presented in Fig. 3b–f, respectively (to our knowledge, the highest values so far for each thickness), whereas the control group without the above improvement steps could achieve conversion efficiencies only in the range 24.28–24.72% (Extended Data Table 1c). Remarkably, the SF cell (125 μm) obtained the highest c-Si solar cell efficiency, and to our knowledge, the FT cell (57 μm) achieved the highest V_{oc} of any c-Si solar cell, 761 mV. The importance of this work is also reflected in

the power-to-weight ratios (PWRs) for each thickness (Fig. 3g). The PWR of the FT cell (57 μm) reached 1.9 W g^{-1} , which, to our knowledge, is the state-of-the-art for c-Si solar cells and more than twice that of the 125- μm SF cell (0.89 W g^{-1}). Meanwhile, the flexibility brought about by thinning was also substantially improved, allowing the cell radius of curvature to be 19.6 mm. This opens up new possibilities for drones, spacecraft and other applications that require extreme weight and flexibility. The advantages of this work can also be seen in a horizontal comparison with other types of solar cell. Extended Data Table 1d lists some representatives of different types of high-performance solar cell. Other current records are those set by Kaneka's interdigitated back contact-structured solar cells (26.7%)^{29,30}, Jinko's tunnel oxide passivated contact solar cells (26.1–26.4%)^{31–33} and LONGi and Trina's passivated emitter and rear contact solar cells (24.06–24.5%)^{34,35}.

External quantum efficiency and stability test

The cell thinning brings two benefits, as evidenced in the absolute efficiency loss model using the theoretical limit (29.1%) as a benchmark (Fig. 4a). First, the resistance of the silicon matrix is reduced, lowering the resistive loss from 0.37% (125 μm) to 0.31% (57 μm). Second, the migration distance of the photogenerated carriers is reduced, lowering the recombination probability, and the extrinsic recombination loss decreases from 0.49% (125 μm) to 0.46% (57 μm). As a consequence, from Fig. 4b we can see that the external quantum efficiency increased with the cell thinning in the ultraviolet-to-visible (UV-Vis) region, on the basis of the shallow absorption depth ($<10 \mu\text{m}$) of the UV-Vis photons. However, the absorption depths of near-infrared (NIR) light exceed the cell thicknesses (for example, 10^2 – $10^6 \mu\text{m}$ at 1,000–1,200 nm), so the external quantum efficiency in the NIR range decreased as cell thinning progressed, increasing the optical loss from 1.44% (125 μm) to 2.27% (57 μm), which is the main cause of the J_{sc} drop with cell thinning. As shown in Fig. 4c, the NIR loss of the FT cell (57 μm) was 0.35 mA cm^{-2} higher than that of the SF cell (125 μm), whereas the thinnest FT cell had the lowest blue (UV-Vis) loss, which was 0.22 mA cm^{-2} lower than

that of the cell with the best PCE. Furthermore, owing to the advanced LTP process, the shading loss was reduced to 1.7%. In addition, the base collection loss, antireflection coating loss and front surface escape loss for the 57- μm cell were also well controlled, accounting for 0.28%, 2.6% and 2.9% respectively, as shown in Fig. 4d,e.

To comprehensively study the cell performance, we systematically investigated the stabilities of the FT and SF SHJ solar cells according to International Electrotechnical Commission 61215:2021 (ref. 36). After 96 h of potential-induced degradation (PID) ageing test (Extended Data Fig. 6), the power attenuation of the FT and SF cells was about 0.6% (Fig. 4f), much lower than the threshold value (5%). At the same time, we also found that the anti-PID capacities of the FT and SF cells exceeded those of the conventional SHJ cells because the reactive plasma deposition-derived ICO layer exhibited electrical properties superior to those of the conventional indium tin oxide layer, as demonstrated in Extended Data Table 1d and Extended Data Fig. 7a,b. Additionally, in the process of light-induced degradation ageing tests, the attenuation should not be higher than 1% after an accumulated illumination of 20 kWh m⁻². As shown in Fig. 4g, the practical power attenuation of the FT and SF cells was still <0.4% after irradiation of 210 kWh m⁻², which was lower than that of the conventional SHJ cells (0.67%) owing to the strengthened i:a-SiO_x:H (1)/a-Si:H (2) composite passivation layers and nanocrystalline n⁺:nc-SiO_x:H and p⁺:nc-Si:H contacts (Extended Data Fig. 7c,d). The results presented above demonstrate that the FT and SF cells are environmentally adaptable and durable. In addition, we observed an intriguing phenomenon: light-induced degradation followed by a degree of PCE recovery, primarily due to the rebound of V_{OC} and FF, whereas J_{SC} remained relatively stable (Extended Data Fig. 8). The underlying causal mechanisms of the light-induced degradation are extremely complicated, and further research and in-depth study are needed. Nevertheless, according to our current research, strengthening the passivation layers and decreasing the overall amorphous degree are effective ways to reduce the impact of light-induced degradation. Another advantage of our structures is the lower cost of the raw material. According to recent SHJ solar cell cost models, every 10 μm of thinning brought about by the FT and SF cells can reduce silicon usage by about 7% and save about 3% in overall manufacturing cost^{2,37–39}.

Online content

Any methods, additional references, Nature Portfolio reporting summaries, source data, extended data, supplementary information, acknowledgements, peer review information; details of author contributions and competing interests; and statements of data and code availability are available at <https://doi.org/10.1038/s41586-023-06948-y>.

- Ballif, C., Haug, F.-J., Boccard, M., Verlinden, P. J. & Hahn, G. Status and perspectives of crystalline silicon photovoltaics in research and industry. *Nat. Rev. Mater.* **7**, 597–616 (2022).
- Razzaq, A., Allen, T. G., Liu, W., Liu, Z. & De Wolf, S. Silicon heterojunction solar cells: techno-economic assessment and opportunities. *Joule* **6**, 514–542 (2022).
- Saga, T. Advances in crystalline silicon solar cell technology for industrial mass production. *NPG Asia Mater.* **2**, 96–102 (2010).
- Solar PV. IEA <https://www.iea.org/reports/solar-pv> (2022).
- Liu, R., Wang, Z. L., Fukuda, K. & Someya, T. Flexible self-charging power sources. *Nat. Rev. Mater.* **7**, 870–886 (2022).
- Massiot, I., Cattoni, A. & Collin, S. Progress and prospects for ultrathin solar cells. *Nat. Energy* **5**, 959–972 (2020).
- Tohoda, S. et al. Future directions for higher-efficiency HIT solar cells using a thin silicon wafer. *J. Non-Cryst. Solids* **358**, 2219–2222 (2012).
- Sai, H., Umishio, H. & Matsui, T. Very thin (56 μm) silicon heterojunction solar cells with an efficiency of 23.3% and an open-circuit voltage of 754 mV. *Sol. RRL* **5**, 2100634 (2021).
- Herasimenka, S. Y., Dauksher, W. J. & Bowden, S. G. >750 mV open circuit voltage measured on 50 μm thick silicon heterojunction solar cell. *Appl. Phys. Lett.* **103**, 053511 (2013).
- Sai, H. et al. Potential of very thin and high-efficiency silicon heterojunction solar cells. *Prog. Photovolt.* **27**, 1061–1070 (2019).
- Liu, W. et al. Flexible solar cells based on foldable silicon wafers with blunted edges. *Nature* **617**, 717–723 (2023).
- Taguchi, M. et al. 24.7% record efficiency HIT solar cell on thin silicon wafer. *IEEE J. Photovolt.* **4**, 96–99 (2014).
- Himalaya HJT solar cell. *Anhui Huasun Energy Co.* <https://www.huasunsolar.com/products/hjt-solar-cell/> (2022).
- Richter, A. et al. Design rules for high-efficiency both-sides-contacted silicon solar cells with balanced charge carrier transport and recombination losses. *Nat. Energy* **6**, 429–438 (2021).
- Qu, X. et al. Identification of embedded nanotwins at c-Si/a-Si:H interface limiting the performance of high-efficiency silicon heterojunction solar cells. *Nat. Energy* **6**, 194–202 (2021).
- You, J. et al. Hydrogen-rich c-Si interfacial modification to obtain efficient passivation for silicon heterojunction solar cell. *J. Mater. Sci.* **31**, 14608–14613 (2020).
- Wang, J. et al. Performance of heterojunction solar cells with different intrinsic a-Si:H thin layers deposited by RF- and VHF-PECVD. *J. Mater. Sci.* **32**, 25327–25331 (2021).
- Ru, X. et al. 25.11% efficiency silicon heterojunction solar cell with low deposition rate intrinsic amorphous silicon buffer layers. *Sol. Energy Mater. Sol. Cells* **215**, 110643 (2020).
- Fujiwara, H., Kaneko, T. & Kondo, M. Application of hydrogenated amorphous silicon oxide layers to c-Si heterojunction solar cells. *Appl. Phys. Lett.* **91**, 133508 (2007).
- Seif, J. P. et al. Strategies for doped nanocrystalline silicon integration in silicon heterojunction solar cells. *IEEE J. Photovolt.* **6**, 1132–1140 (2016).
- Lei, C. et al. Phosphorus treatment to promote crystallinity of the microcrystalline silicon front contact layers for highly efficient heterojunction solar cells. *Sol. Energy Mater. Sol. Cells* **209**, 110439 (2020).
- Mazzarella, L. et al. Nanocrystalline n-type silicon oxide front contacts for silicon heterojunction solar cells: photocurrent enhancement on planar and textured substrates. *IEEE J. Photovolt.* **8**, 70–78 (2018).
- Zhao, Y. et al. Design and optimization of hole collectors based on nc-SiO_x:H for high-efficiency silicon heterojunction solar cells. *Sol. Energy Mater. Sol. Cells* **219**, 110779 (2021).
- Zhang, L. et al. Cerium-doped indium oxide as a top electrode of semitransparent perovskite solar cells. *ACS Appl. Mater. Interfaces* **15**, 10838–10846 (2023).
- Kobayashi, E., Watabe, Y. & Yamamoto, T. High-mobility transparent conductive thin films of cerium-doped hydrogenated indium oxide. *Appl. Phys. Express* **8**, 015505 (2015).
- Han, C. et al. Towards bifacial silicon heterojunction solar cells with reduced TCO use. *Prog. Photovolt.* **30**, 750–762 (2022).
- Adrian, A., Rudolph, D., Willenbacher, N. & Lossen, J. Finger metallization using pattern transfer printing technology for c-Si solar cell. *IEEE J. Photovolt.* **10**, 1290–1298 (2020).
- Adachi, D., Hernández, J. L. & Yamamoto, K. Impact of carrier recombination on fill factor for large area heterojunction crystalline silicon solar cell with 25.1% efficiency. *Appl. Phys. Lett.* **107**, 233506 (2015).
- Green, M. A. et al. Solar cell efficiency tables (version 61). *Prog. Photovolt.* **31**, 3–16 (2023).
- Yoshikawa, K. et al. Silicon heterojunction solar cell with interdigitated back contacts for a photoconversion efficiency over 26%. *Nat. Energy* **2**, 17032 (2017).
- Zhang, X. et al. Mass production of crystalline silicon solar cells with polysilicon-based passivating contacts: an industrial perspective. *Prog. Photovolt.* **31**, 369–379 (2023).
- JinkoSolar's high-efficiency n-type monocrystalline silicon solar cell sets our new record with maximum conversion efficiency of 26.1%. *Jinko Solar* <https://www.jinkosolar.com/en/site/newsdetail/1775> (2022).
- JinkoSolar's high-efficiency n-type monocrystalline silicon solar cell sets our new record with maximum conversion efficiency of 26.4%. *Jinko Solar* <https://www.jinkosolar.com/en/site/newsdetail/1827> (2022).
- LONGi Solar sets new bifacial mono-PERC solar cell world record at 24.06 percent. *LONGi Solar* <https://www.longi.com/en/news/6821/> (2019).
- 210 PERC cell efficiency achieves 24.5%, Trina Solar breaks world record for the 24th time. *Trina Solar* <https://www.trinasolar.com/en-gb/resources/newsroom/en210-perc-cell-efficiency-achieves-245-trina-solar-breaks-world-record-24th-time> (2022).
- Repins, I. L., Kersten, F., Hallam, B., VanSant, K. & Koentopp, M. B. Stabilization of light-induced effects in Si modules for IEC 61215 design qualification. *Sol. Energy* **208**, 894–904 (2020).
- Louwen, A., van Sark, W., Schropp, R. & Faaij, A. A cost roadmap for silicon heterojunction solar cells. *Sol. Energy Mater. Sol. Cells* **147**, 295–314 (2016).
- Green, M. A. et al. Solar cell efficiency tables (version 62). *Prog. Photovolt.* **31**, 651–663 (2023).
- Yoshikawa, K. et al. Exceeding conversion efficiency of 26% by heterojunction interdigitated back contact solar cell with thin film Si technology. *Sol. Energy Mater. Sol. Cells* **173**, 37–42 (2017).

Publisher's note Springer Nature remains neutral with regard to jurisdictional claims in published maps and institutional affiliations.

Springer Nature or its licensor (e.g. a society or other partner) holds exclusive rights to this article under a publishing agreement with the author(s) or other rightsholder(s); author self-archiving of the accepted manuscript version of this article is solely governed by the terms of such publishing agreement and applicable law.

© The Author(s), under exclusive licence to Springer Nature Limited 2024

Methods

Preprocessing

As-cut 150- μm M6 size ($166 \times 166 \text{ mm} \pm 0.25$) n-type Czochralski c-Si wafers were further thinned to 55–130 μm for cell fabrication. The wafers were in (100) orientation with a resistivity of 1–3 $\Omega \text{ cm}$. The thinning process was conducted by immersing the wafers in 10% KOH-based solution for isotropic chemical etching. The etching duration was carefully controlled from 180 to 1,500 s to obtain the target wafer thicknesses. Subsequently, the wafers were textured in KOH solution mixed with additives. Pyramids featuring (111)-orientated facets and 3–9 μm in size were formed on both sides after texturing, followed by chemical removal with a 1–2% diluted hydrofluoric acid solution for stripping off native SiO_x films on the wafer surface. The average thickness of each set of wafers was determined by weight measurement with an accuracy of $\pm 0.5 \mu\text{m}$.

Surface passivation

The feed gases of silane (SiH_4) and carbon dioxide (CO_2) with a flow ratio of $[\text{CO}_2]/[\text{SiH}_4] = 0.15:1$ were induced by the RF PECVD (13.56 MHz) system at 190 $^\circ\text{C}$ to grow 2–3 atomic and epitaxy-preventing i:a- SiO_x :H (1) subnanolayers ($< 0.5 \text{ nm}$) on both sides. To avoid unwanted plasma damage during the implementation of subsequent passivation layers, we installed a self-developed continuous regulation and control system (CRCS) in the CVD equipment; $> 5,000$ diodes were integrated in CRCS as the feedback terminal for real-time monitoring of plasma bombardment intensity, particularly surface voltage, on the whole cell surface ($166 \times 166 \text{ mm}$), cooperating with the fine adjustment from the intelligent control system in CRCS to balance the system resistance and avoid plasma fluctuations. Therefore, we found that not only can the plasma be kept uninterrupted during the feed gas switching process, but also the plasma fluctuations can be controlled at a low level during the entire passivation process, especially important in transitional periods. Then, the CO_2 supply was programmatically switched to hydrogen (H_2) until a flow ratio of $[\text{H}_2]/[\text{SiH}_4] = 19:1$; Extended Data Fig. 9a verifies that the plasma fluctuation was controlled $< \pm 0.5\%$ under precise CRCS adjustment. Subsequently, another approximately 4.5-nm-thick epitaxy-free i:a-Si:H (2) layer was coated onto the i:a- SiO_x :H (1) subnanolayers bifacially. The continuous-plasma CVD process produces a natural interface transition from the first passivation layer to the second passivation layer, and the entire passivation process protects the delicate amorphous layers from plasma damage.

By contrast, conventional passivation relies on the step-by-step PECVD processes for depositing multiple layers, which are susceptible to contamination and defects (bombardment damage). For comparison with the continuous-plasma CVD process, we prepared the control group as follows. The i:a- SiO_x :H (1) layers were grown in the same way as above; however, we found that without the rapid-response regulation of CRCS, the plasma fluctuation in the conventional CVD process was about 8% (Extended Data Fig. 9b), inferring that the uniformity of the resulting passivation layers is inferior to that of those produced through the continuous-plasma CVD process. More seriously, in conventional CVD passivation, switching between different feed gases causes a sudden change of system resistance, rendering the plasma unsustainable and the RF power to cease after depositing the i:a- SiO_x :H (1) subnanolayers. Until the feed gases were switched to the predetermined proportion of $[\text{H}_2]/[\text{SiH}_4] = 19:1$, RF plasma was reignited along with high-voltage pulses (Extended Data Fig. 9c) and the power was rematched to deposit the subsequent i:a-Si:H (2) passivation layer.

Doped contacts, TCO and grid lines

The doped contact layers were fabricated through self-restoring nanocrystalline sowing and vertical growth induction. The i:a-Si:H (2) surfaces were intentionally pretreated with a bifunctional plasma of CO_2 and H_2 mixture through VHF PECVD (40.68 MHz) for 20–50 s,

with a flow ratio of $[\text{CO}_2]/[\text{H}_2] = 1:20$, to sow nanocrystalline seeds and preserve hydrogen contents in the passivation layers, maintaining the optimal passivation effect while restricting microcrystalline sowing on the shallow surfaces and inducing vertical growth of the subsequent doped nanocrystalline junctions. On this foundation, high-quality n- and p-type carrier-selective contacts can be achieved. Briefly, a 15-nm phosphorus-doped front n-type window layer (n^+ :nc- SiO_x :H) grew on i:a-Si:H (2) as an electron collecting layer at a high hydrogen-to-silane gas-flow ratio of $[\text{H}_2]/[\text{SiH}_4]/[\text{PH}_3] = 750:5:0.1$, with $[\text{CO}_2]/[\text{SiH}_4] = 0.5 \pm 0.2$ to balance the crystallinity fraction and optical bandgap. For the rear junction, the hydrogen-to-silane gas-flow ratio was further increased to $[\text{H}_2]/[\text{SiH}_4]/[\text{B}_2\text{H}_6] = 2,700:5:0.1$, implementing a 22-nm boron-doped p^+ :nc-Si:H film with an ultrahigh X_c of 63.4%. The n^+ :nc- SiO_x :H and p^+ :nc-Si:H contacts were grown in the same chamber at a substrate temperature of 170 $^\circ\text{C}$. Afterwards, a 2.8% Ce-doped In_2O_3 (ICO) target was applied for depositing approximately 70-nm TCO layers on both sides in a low-damage reactive plasma deposition sputtering tool by using high-purity Ar as the sputtering gas at a substrate temperature of 100 $^\circ\text{C}$, and the coating process was less than 30 eV ion bombardment, without damaging the microcrystalline emitters and the passivation layers. The contact-free LTP was carried out for grid lines with a line width of 18 μm and the aspect ratio was optimized to 0.7. For certificated cells, an 80-nm MgF_2 layer was capped onto the front side in a thermal evaporation instrument (ULVAC, EI-501Z).

Characterization

Current–voltage (I – V) characteristics of the solar cells were measured by a Vision VS-6821S I – V tester under standard test conditions (AM1.5 G, 100 mW cm^{-2} , 25 $^\circ\text{C}$). The best SHJ solar cells were certified through total area measurement by the Institute for Solar Energy Research in Hamelin. External quantum efficiency spectra were measured on the entire front surface including the grid-shaded area with a Bentham PVE300-IVT system and QE-RX (Enlitech), and the corresponding optical loss was analysed using SQ-JVFL. HRTEM was conducted in an FEI Titan 80–300 Berlin Holography Special TEM and TF-G20 (Thermo Fisher), for which the cross-sectional samples were prepared by a focused ion beam technique. The atomic force microscopy images and morphology features were obtained with semi-contact mode and an OMCL-AC200TS cantilever probe by Ntegra Prima. Crystallinity fractions (X_c), also called crystalline volume fractions, were extracted by Raman spectroscopy with a 325-nm UV light generated by a He–Cd laser, using a fitting Gaussian model. The optical characteristics of the layers, including absorbance, reflectance and transmittance, were measured using UV–Vis–NIR spectroscopy (Perkin Elmer Lambda 950), and the bandgaps (E_g) of the layers were calculated from the Tauc plots. The minority carrier lifetime was obtained by a Sinton WCT-120 flash tester in transient mode. The vertical conductivities (σ_y) of the doped contacts, rather than the horizontal conductivities (σ_x), were detected by a self-built probe system, because the charges move vertically in the cells. Traditional doped a-Si:H layers are homogeneous (that is, isotropic ($\sigma_y = \sigma_x$)), and it is rational and more convenient to probe σ_x instead of σ_y . However, the nanocrystalline sowing and vertical growth induction process induces an oriented growth, producing anisotropic doped contacts ($\sigma_y > \sigma_x$), which causes unacceptable error if σ_x is used instead of σ_y . A Hall measurement system (Ecopia, HMS-3000) was used to determine the carrier mobility and conductivity of the TCO layers. The hydrogen content (C_H) and microstructure factor (R') were calculated from Fourier transform infrared responses captured by a Nicolet IS-10 spectrometer according to the following formulae.

$$C_H = \frac{N_H}{N_H + N_{Si}}$$

$$N_H = A_{2000} \times I_{2000} + A_{2100} \times I_{2100}$$

$$R^* = \frac{I_{2100}}{I_{2000} + I_{2100}}$$

in which N_{H} is the atomic density of hydrogen, $N_{\text{Si}} = 5 \times 10^{22} \text{ cm}^{-3}$ is the atomic density of pure silicon, $A_{2000} = 9.0 \times 10^{19} \text{ cm}^{-2}$ and $A_{2100} = 2.2 \times 10^{20} \text{ cm}^{-2}$ are proportionality constants with the hydrogen stretching mode at $2,000 \text{ cm}^{-1}$ and $2,100 \text{ cm}^{-1}$, and I_{2000} and I_{2100} are the integrated absorption peak intensities at $2,000$ and $2,100 \text{ cm}^{-1}$, respectively.

Flexibility analysis and measurement

The static structural module in the Ansys WORKBENCH software was used to simulate the flexibility of the $166 \times 166 \text{ mm}$ c-Si solar cells. The cell models were built in the Design Modeler, with an arc length of 166 mm and an initial 500 mm radius of curvature in the z - x plane, and the one-dimensional 166-mm curves were extruded in the y direction to form two-dimensional curved surface geometries. Inputting the parameters (density: $2,330 \text{ kg m}^{-3}$, Young's modulus: 187 GPa , Poisson's ratio: 0.28 , yield strength: 7 GPa , tangent modulus: 63.7 GPa , tensile yield strength: 350 MPa) to the surface geometries, which were divided into 3-mm surface mesh in the Mechanical. Following that, remote displacement constraints in the y direction were applied to each of the straight edges, allowing displacement only in the x direction and rotation only in the y direction, and the two straight edges were loaded with a horizontal force towards the centre. According to the first strength theory, the solar cells fracture when the maximum principal stress exceeds or equals the limit of tensile strength, at which point the deformation of the solar cells in the x and z directions was recorded and the bending angle was calculated. The flexibility measurement of c-Si solar cells was completed by using a self-made programmed symmetrical extrusion system. Servo motors were used to control the relatively slow extrusion speed (1 mm s^{-1}) until the cells were broken, and the corresponding bending angles and radii of curvature were recorded.

The concept of 'bendability' refers to the property of being bent without breaking, which can be quantified by various parameters in different pieces of literature. In this paper, two indices are used for evaluation (that is, the maximum bending angle (θ) and the minimum bending radius of curvature (r_b), and the relation formula is as follows.

$$r_b = \frac{360^\circ \times l}{2 \times \pi \times \theta}$$

in which l is the length of the arc (equal to the cross-sectional edge length 166 mm).

Encapsulation and ageing test

The solar cells were encapsulated with the EPE encapsulant (EVA/POE/EVA = 1:x:1, $x = 1\text{--}1.2$) into the modules, followed by measuring the initial maximum power (P_0). The edges of the modules were attached with conductive copper tapes for grounding. The positive and negative terminals of the modules were connected to the high-voltage output power supply ($-1,500 \text{ V}$). The stability and persistence were tested in a high-temperature (85°C) and high-humidity (85%) ageing chamber (H8-050) for 192 h . Dividing the maximum power after the ageing tests (P_t) by the initial maximum power (P_0), the degree of attenuation can be assessed. A schematic diagram of the PID ageing process can be

found in Extended Data Fig. 6. All of the encapsulation materials were pre-aged in the ageing chamber (UV-plus430 and GRO-SUV1010) at high temperature (85°C) and humidity (85%) with UV illumination ($280\text{--}400 \text{ nm}$, UVB accounts for $3\text{--}10\%$ of the whole energy). The light-induced degradation ageing tests were conducted according to International Electrotechnical Commission 61215:2021.

Absolute efficiency loss analysis

The power and efficiency losses were quantified by Quokka3 simulation. The models of the FT and SF cells were established, and the input parameters such as TCO square resistance, line resistance, TCO/nc-Si(O_x):H/a-Si:H (2)/a-Si O_x :H (1)/c-Si contact resistance, surface recombination rate and so on were directly measured by experimental characterization. From the model and fitting variables, other parameters can be derived, including Auger recombination, radiation recombination and Shockley–Read–Hall recombination. Following convergence of the simulated and measured electrical properties, the efficiency loss components were quantified at the maximum power point. The concepts and calculation details of the theoretical limit and practical limit can be found in the literature³⁰.

Reporting summary

Further information on research design is available in the Nature Portfolio Reporting Summary linked to this article.

Data availability

All data generated or analysed during this study are included in the paper and its extended data files.

Acknowledgements This work has been supported by the National Natural Science Foundation of China (numbers 21606171 and 22179054), the China Postdoctoral Science Foundation (numbers 2021M691326, 2015M580205 and 2017T100160), the Natural Science Foundation of Jiangsu Province (number BK20211345) and the Ministry of Science and Technology of the People's Republic of China (number DL2022014014L). Z.S. acknowledges the support from the Australian Research Council via Discovery Projects (numbers DP200103315, DP200103332 and DP230100685) and Linkage Projects (number LP220200920). Y.L. thanks Baoyu-Huang and Zhengfeng Yang for assistance with the experiments; Jiating Wu and Yuxuan Li for assistance with the preparation for publication; and all group members of X.X. and Z.S. for continuous support. Jiangsu University of Science and Technology and LONGi Green Energy Technology Co., Ltd have equal rights of this work.

Author contributions Y.L. conceived the idea, designed the cells, explored the mechanisms, and wrote and revised the manuscript. X.R. designed the experiments and fabricated the solar cells. M.Y. guided the experimental fabrication technology. Y.Z. was responsible for the flexibility simulation and measurement, figures, tables and preparation for publication. S.Y. and C.H. developed the TCO process. F.P. developed the metallization process and conducted the efficiency certification. M.Q., C.X., J.L. and L.F. managed the project and participated in experiment design. C.S. assisted in characterization and data analysis. D.C., J.X. and C.Y. provided resources and funding support. Z.L. and X.X. organized the research. Z.S. supervised the project.

Competing interests Jiangsu University of Science and Technology is in the process of applying for a Chinese invention patent (202311478687.5) related to the subject matter of this manuscript. Z.L. and X.X. are co-founders of LONGi Central R&D Institute. X.R., M.Y., S.Y., C.H., F.P., M.Q., C.X., J.L. and L.F. are employees of LONGi. The other authors declare no competing interests.

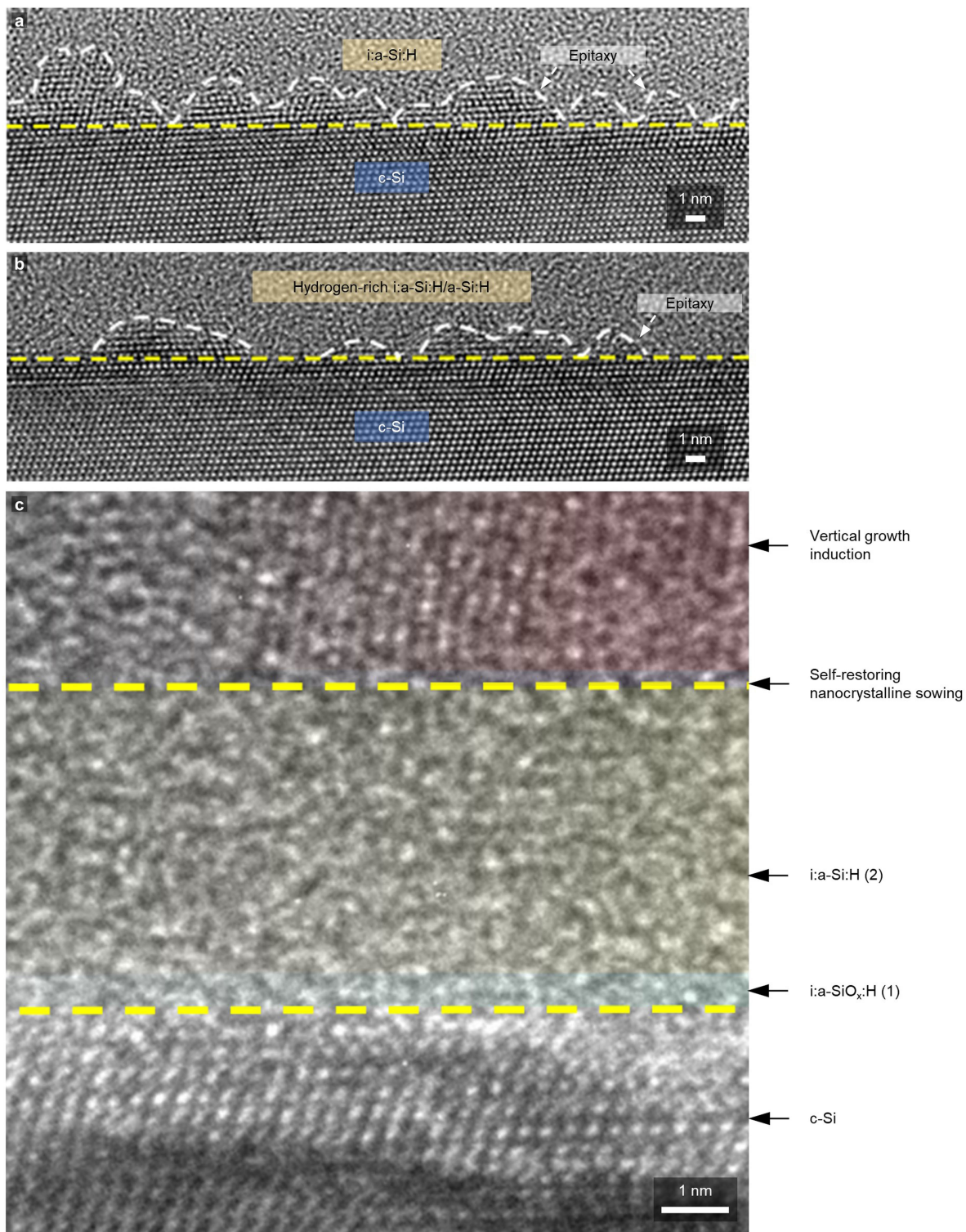
Additional information

Supplementary information The online version contains supplementary material available at <https://doi.org/10.1038/s41586-023-06948-y>.

Correspondence and requests for materials should be addressed to Daifen Chen, Junhua Xu, Chao Yan, Zhenguo Li, Xixiang Xu or Zongping Shao.

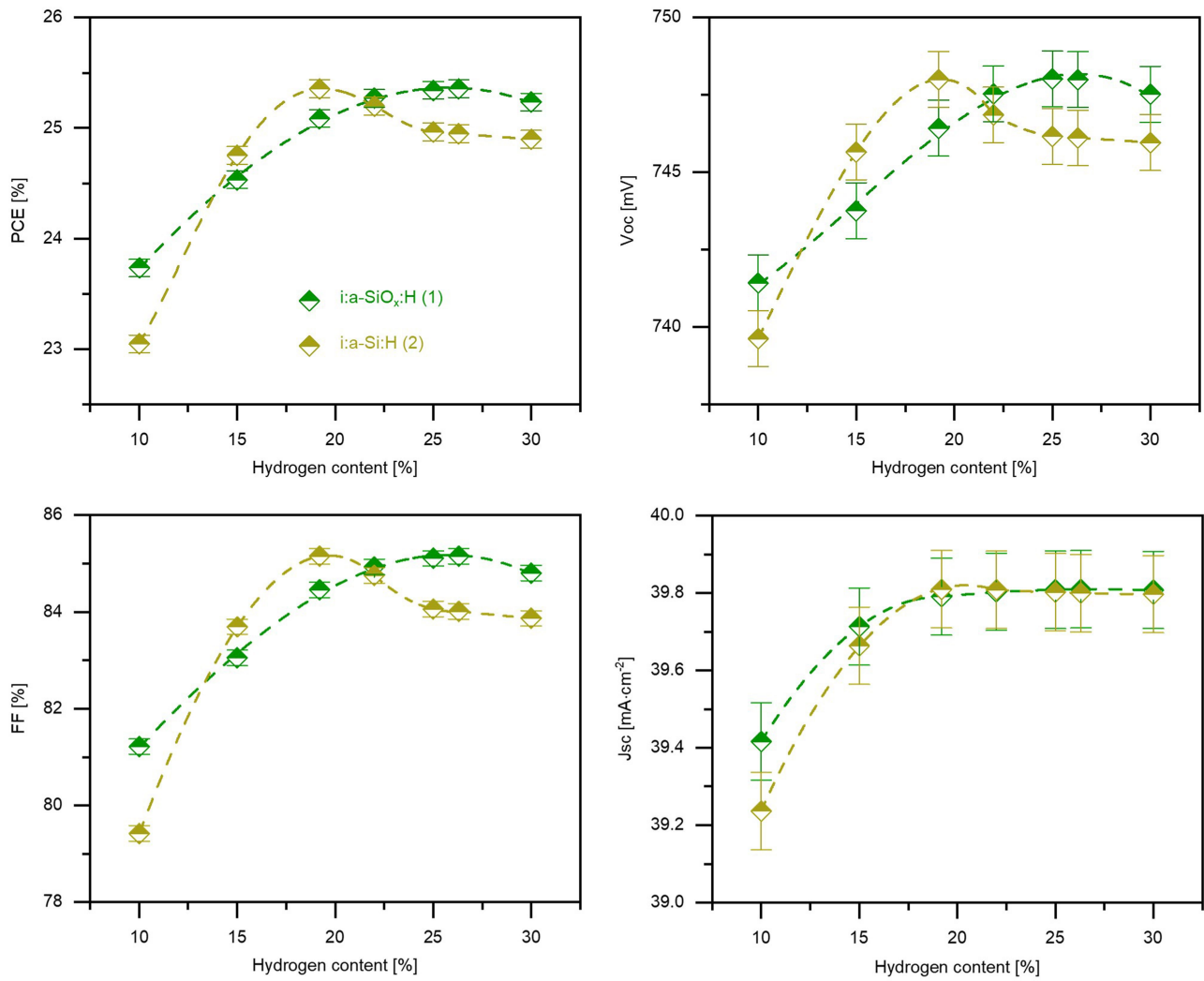
Peer review information Nature thanks Han-Don Um and the other, anonymous, reviewer(s) for their contribution to the peer review of this work.

Reprints and permissions information is available at <http://www.nature.com/reprints>.

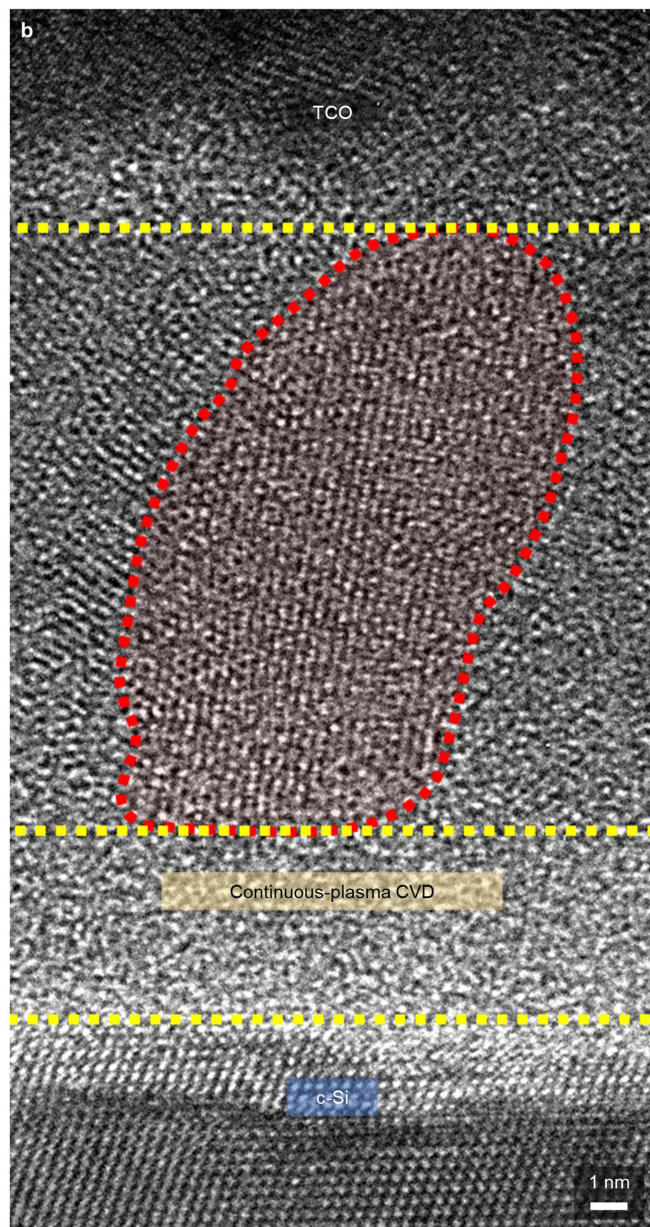
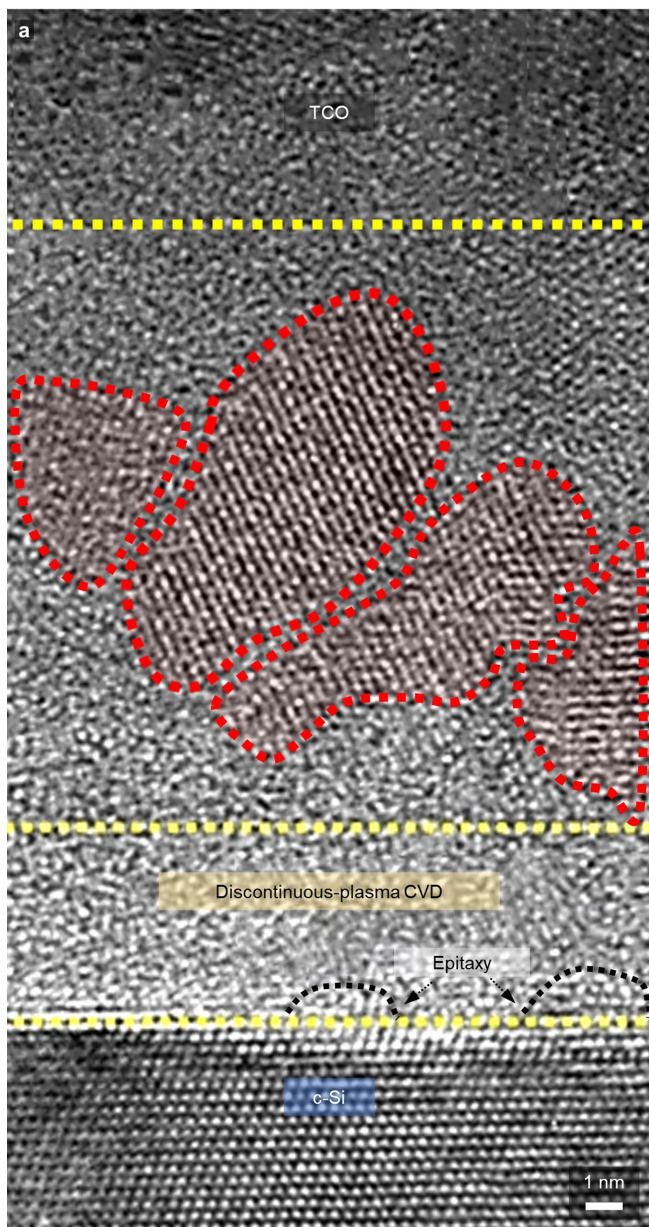


Extended Data Fig. 1 | Cross-sectional HRTEM images. **a**, Cross-sectional morphology of the c-Si/i:a-Si:H interface. **b**, Cross-sectional morphology of c-Si/hydrogen-rich i:a-Si:H/a-Si:H. **c**, Enlarged cross-sectional morphology of

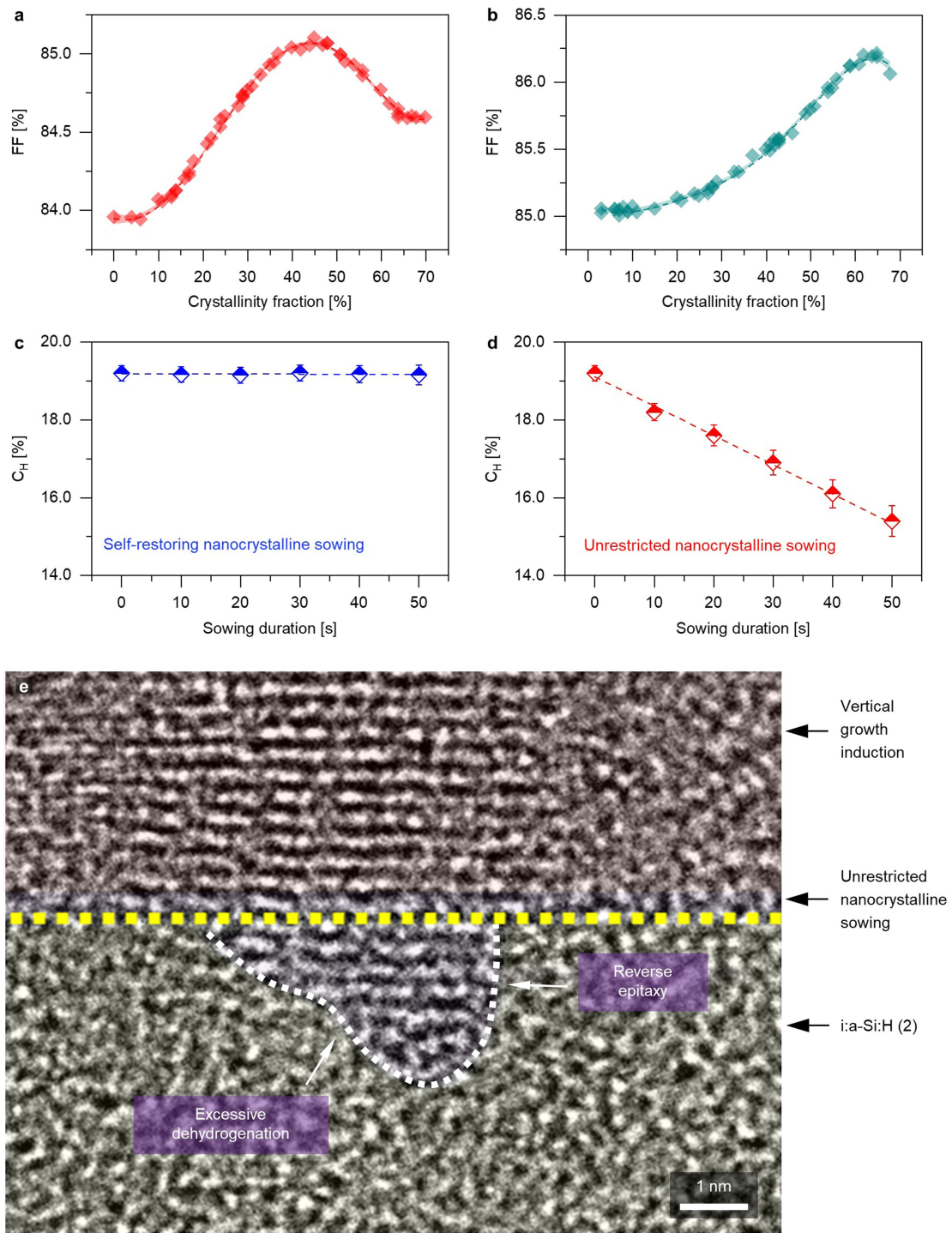
the i:a-SiO_x:H (1)/a-Si:H (2) composite gradient passivation layers prepared via continuous-plasma CVD.



Extended Data Fig. 2 | Hydrogen content. Effect of hydrogen content (C_H) variation in the epitaxy-preventing composite gradient passivation layers on cell performance. The dashed lines in the panels are fit lines to evaluate the data change trends.

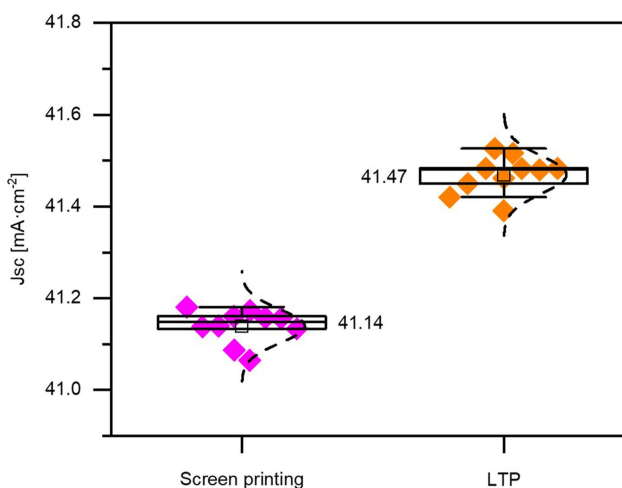
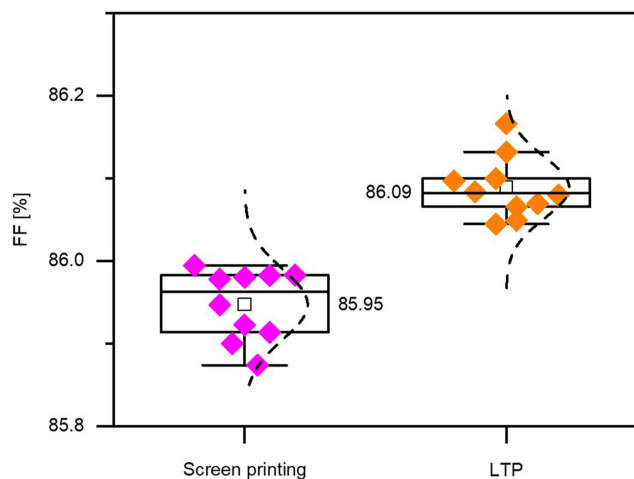
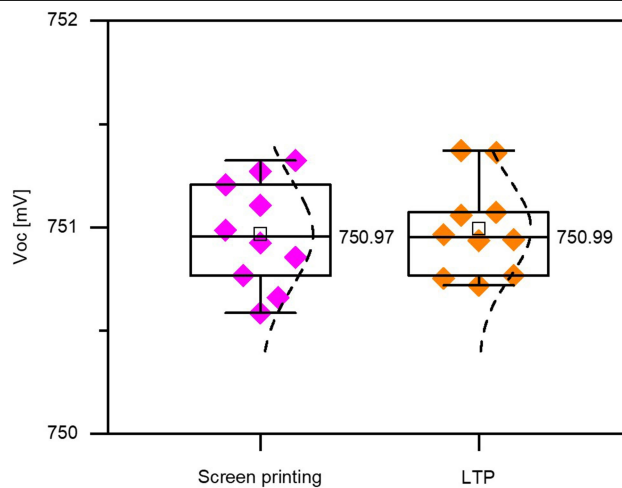
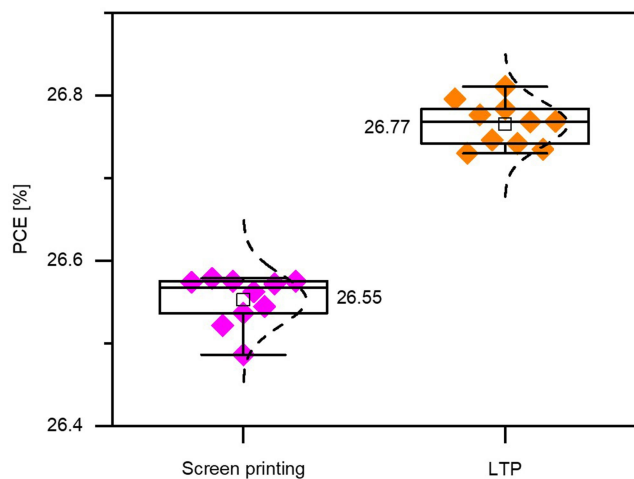


Extended Data Fig. 3 | Self-restoring nanocrystalline sowing and vertical growth induction (NSVGI). **a**, Cross-sectional HRTEM image of the doped contact layer fabricated via conventional random growth. **b**, Cross-sectional HRTEM image of the doped contact layer fabricated via self-restoring NSVGI.



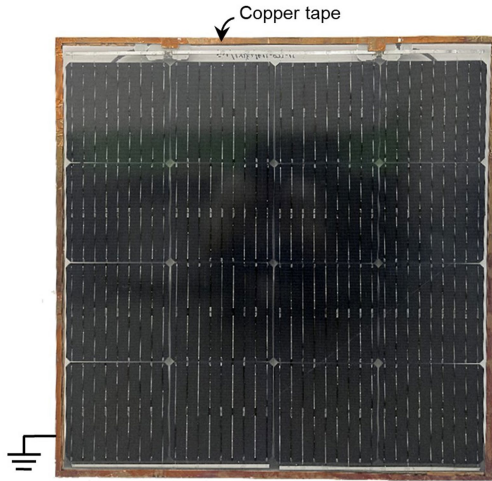
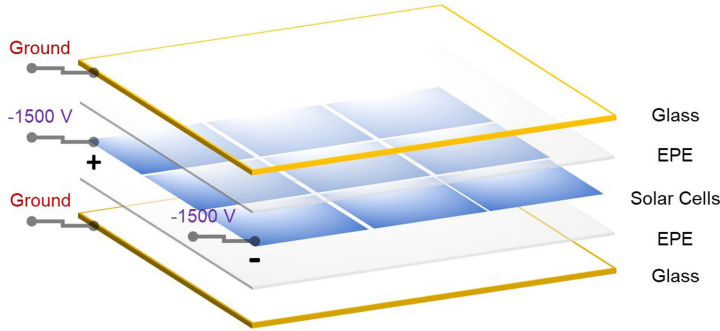
Extended Data Fig. 4 | Self-restoring nanocrystalline sowing. **a**, Relationship between the FF and crystallinity fraction of the n⁺:nc-SiO_x:H window layer with a p⁺:a-Si:H rear emitter. **b**, Relationship between the FF and crystallinity fraction of the p⁺:nc-Si:H rear emitter with the optimal n⁺:nc-SiO_x:H window layer. **c, d**, Variation of C_H in i:a-Si:H (2) with sowing duration via

self-restoring nanocrystalline sowing and unrestricted nanocrystalline sowing, respectively. **e**, Enlarged cross-sectional HRTEM image of i:a-Si:H (2) after the unrestricted nanocrystalline sowing. The dashed lines in the panels (a, b, c, d) are fit lines to evaluate the data change trends.



Extended Data Fig. 5 | Contact-free laser transfer printing. Comparison of the cell performance parameters via conventional screen printing and contact-free laser transfer printing (LTP).

Article



China National Accreditation Service for Conformity Assessment
LABORATORY ACCREDITATION CERTIFICATE
(Registration No. CNAS L8028)

Test Center of Changzhou Sveck Photovoltaic New Material Co., Ltd.

(Legal Entity: Changzhou Sveck Photovoltaic New Material Co., Ltd.)

No.8, Zhili Road, Industrial Park, Zhixi, Jintan District, Changzhou, Jiangsu, China

is accredited in accordance with ISO/IEC 17025: 2017 General Requirements for the Competence of Testing and Calibration Laboratories (CNAS-CL01 Accreditation Criteria for the Competence of Testing and Calibration Laboratories) for the competence to undertake the service described in the schedule attached to this certificate.

The scope of accreditation is detailed in the attached schedule bearing the same registration number as above. The schedule forms an integral part of this certificate.

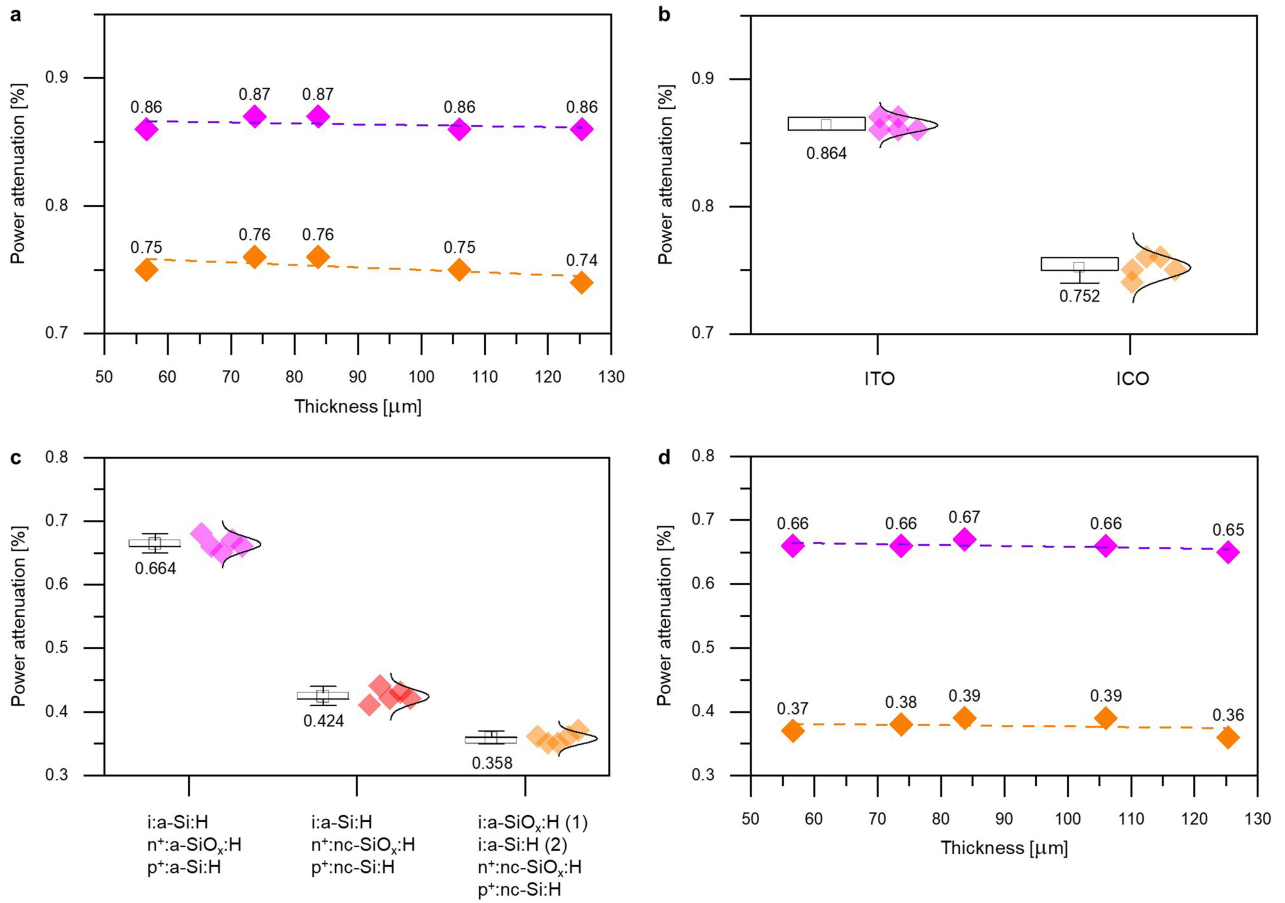
Effective Date: 2020-11-03

Expiry Date: 2024-10-20

Signed on behalf of China National Accreditation Service for Conformity Assessment

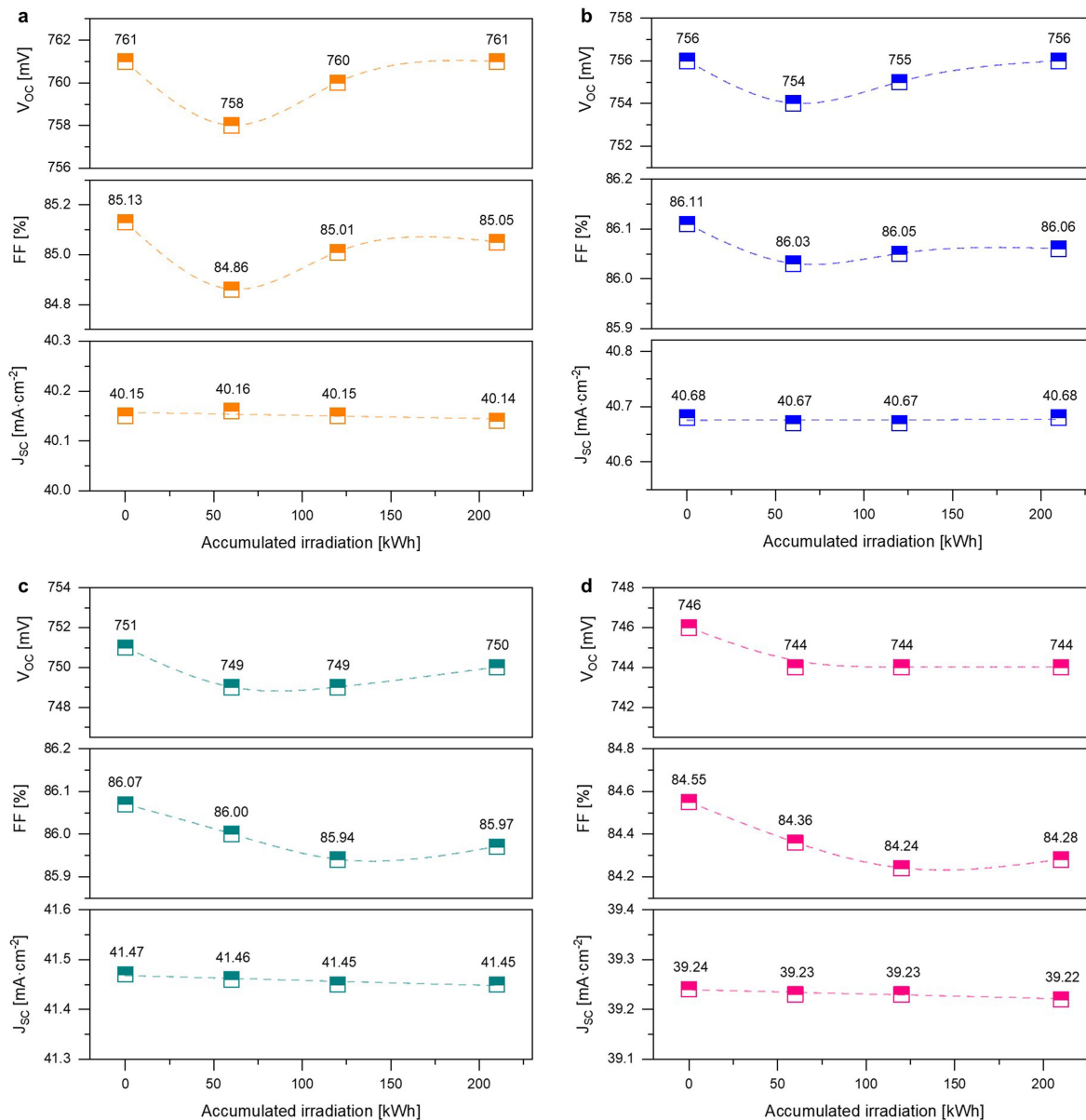
China National Accreditation Service for Conformity Assessment (CNAS) is authorized by Certification and Accreditation Administration of the People's Republic of China (CACA) to operate the national accreditation schemes for conformity assessment. CNAS is a signatory of the International Laboratory Accreditation Cooperation Mutual Recognition Arrangement (ILAC MRA) and the Asia Pacific Accreditation Cooperation Mutual Recognition Arrangement (APAC MRA). The validity of the certificate can be checked on CNAS website at <http://www.cnas.org.cn/english/findaccreditedbody/index.shtml>.

Extended Data Fig. 6 | Endurance assessment. Encapsulation schematics for the SF and FT SHJ modules, as well as the laboratory accreditation certificate for the third-party assessment. The certificate is reproduced with permission from Changzhou Sveck Photovoltaic New Material Co., Ltd.



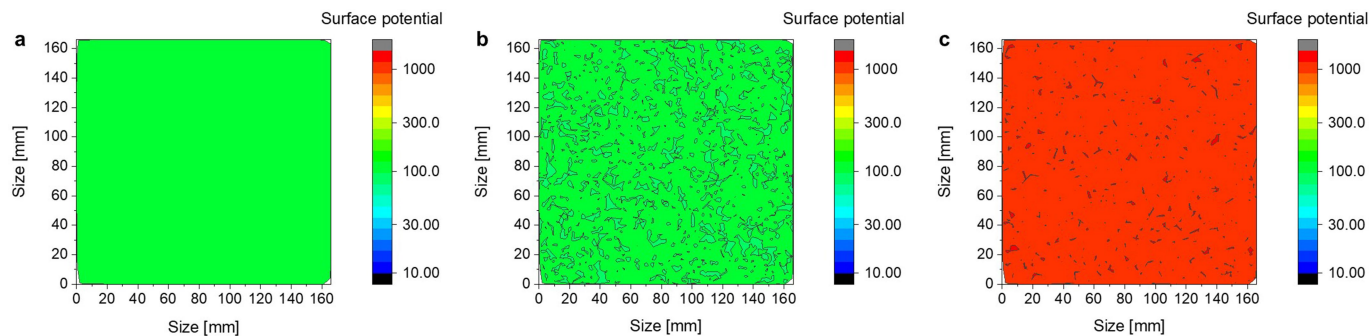
Extended Data Fig. 7 | Durability analysis. **a**, Impact of the different TCO layers on the PID resistance of the FT and SF SHJ cells for each thickness. **b**, Statistical analysis of the anti-PID capacities of the FT and SF cells with the ITO and ICO layers. Temperature: 85 °C, humidity: 85%, bias: -1,500 V, duration: 192 h. **c**, Statistical analysis of the anti-light-induced degradation capacities of

the FT and SF cells with the different passivation and contact layers. **d**, Light-induced degradation resistance of the FT and SF cells for each thickness. Accumulated illumination of 210 kWh·m⁻². The dashed lines in the panels (a, d) are fit lines to evaluate the data change trends.



Extended Data Fig. 8 | Power recovery in light-induced degradation. a, V_{OC} , FF, J_{SC} variation of the FT (57 μm) cell during light-induced degradation ageing. **b,** V_{OC} , FF, J_{SC} variation of the FT (84 μm) cell during light-induced degradation ageing. **c,** V_{OC} , FF, J_{SC} variation of the SF (125 μm) cell during light-induced

degradation ageing. **d,** V_{OC} , FF, J_{SC} variation of the conventional SHJ (150 μm) cell during light-induced degradation ageing. The dashed lines in the panels are fit lines to evaluate the data change trends.



Extended Data Fig. 9 | Visualization of the surface potential distribution during RF-PECVD. a, Continuous-plasma CVD process with CRCS (fluctuation $< \pm 0.5\%$). **b,** Conventional discontinuous-plasma CVD passivation (fluctuation $< \pm 8\%$). **c,** Conventional discontinuous-plasma CVD passivation at the reignition moment.

Extended Data Table 1 | Evaluation of the performance using various technologies

a

Passivation layers	Configuration	τ_{eff} (ms)	Operation procedures
i:a-Si:H	Single	2.8 ± 0.2	/
Hydrogen-rich i:a-Si:H	Single	3.3 ± 0.2	/
Hydrogen-rich i:a-Si:H/a-Si:H	Composite	4.1 ± 0.3	Discontinuous-plasma CVD
Hydrogen-rich i:a-Si:H/a-Si:H	Composite	4.5 ± 0.3	Continuous-plasma CVD
i:a-SiO _x :H (1)/a-Si:H (2)	Composite	4.4 ± 0.3	Discontinuous-plasma CVD
i:a-SiO _x :H (1)/a-Si:H (2)	Composite	5.0 ± 0.3	Continuous-plasma CVD

b

TCO	ITO	ICO
Preparation method	Magnetron sputtering	Low-damage RPD
Thickness (nm)	70	70
Planar resistivity ($\Omega \cdot \text{cm}$)	1.2×10^{-3}	2.7×10^{-4}
Mobility ($\text{cm}^2 \text{V}^{-1} \text{s}^{-1}$)	31.5	83.1
PID after 192 h (%)	0.86	0.75

c

Thickness (μm)	V_{oc} (V)	J_{sc} ($\text{mA} \cdot \text{cm}^{-2}$)	FF (%)	PCE (%)
57	0.754	38.29	84.11	24.28
74	0.752	38.48	84.29	24.39
84	0.751	38.73	84.50	24.58
106	0.748	38.99	84.51	24.64
125	0.746	39.20	84.55	24.72

Passivation layers: Hydrogen-rich i:a-Si:H/a-Si:H

Passivation method: Discontinuous-plasma CVD

Carrier selective contacts: Random nanocrystalline growth

Grid lines: Screen printing

d

Cell type	c-Si thickness (μm)	V_{oc} (V)	J_{sc} ($\text{mA} \cdot \text{cm}^{-2}$)	FF (%)	PCE (%)	Area (cm^2)	Reference
FT SHJ	84	0.756	40.72	86.11	26.50	274.4	This work
SF SHJ	125	0.751	41.45	86.07	26.81	274.4	This work
PERC	170	0.694	41.58	83.30	24.00	244.6	29
PERC	400	0.706	42.70	82.80	25.00	4	38
TOPCon	200	0.732	42.00	84.30	26.00	4	14
IBC-SHJ	165	0.744	42.30	83.80	26.30	180.4	30
IBC-SHJ	200	0.740	42.50	84.60	26.60	179.7	39

a, Effect of the different passivation layers on effective minority carrier lifetime. **b**, Electrical properties of the different TCO layers and their effects on PID resistance. **c**, Performance parameters of the reference cells manufactured via conventional techniques. **d**, Comparison of the FT and SF SHJ solar cells with other types of advanced solar cells.

Solar Cells Reporting Summary

Nature Research wishes to improve the reproducibility of the work that we publish. This form is intended for publication with all accepted papers reporting the characterization of photovoltaic devices and provides structure for consistency and transparency in reporting. Some list items might not apply to an individual manuscript, but all fields must be completed for clarity.

For further information on Nature Research policies, including our [data availability policy](#), see [Authors & Referees](#).

▶ Experimental design

Please check: are the following details reported in the manuscript?

1. Dimensions

- Area of the tested solar cells Yes 274.4 cm²
 No
- Method used to determine the device area Yes Full area of 274.4 cm² defined by self-testing and the Institute for Solar Energy Research in Hamelin (ISFH) certification.
 No

2. Current-voltage characterization

- Current density-voltage (J-V) plots in both forward and backward direction Yes Same J-V curves were obtained in forward and backward directions for c-Si solar cells.
 No
- Voltage scan conditions Yes There are no special restriction on the voltage scan direction, speed or dwell time.
For instance: scan direction, speed, dwell times No
- Test environment Yes Standard test conditions (25°C, AM 1.5G in air).
For instance: characterization temperature, in air or in glove box No
- Protocol for preconditioning of the device before its characterization Yes Not essential.
 No
- Stability of the J-V characteristic Yes The potential-induced degradation (PID) and light-induced degradation aging tests confirm that the FT and SF SHJ solar cells have sufficient reliability.
Verified with time evolution of the maximum power point or with the photocurrent at maximum power point; see ref. 7 for details. No

3. Hysteresis or any other unusual behaviour

- Description of the unusual behaviour observed during the characterization Yes No behaviours of hysteresis were observed.
 No
- Related experimental data Yes No behaviours of hysteresis were observed.
 No

4. Efficiency

- External quantum efficiency (EQE) or incident photons to current efficiency (IPCE) Yes External quantum efficiency (EQE) data are shown in Figure 4b.
 No
- A comparison between the integrated response under the standard reference spectrum and the response measure under the simulator Yes Not essential. All of the reported cells were certified by the Institute for Solar Energy Research in Hamelin (ISFH).
 No
- For tandem solar cells, the bias illumination and bias voltage used for each subcell Yes Not relevant.
 No

5. Calibration

- Light source and reference cell or sensor used for the characterization Yes Certified by the Institute for Solar Energy Research in Hamelin (ISFH).
 No
- Confirmation that the reference cell was calibrated and certified Yes Certified by the Institute for Solar Energy Research in Hamelin (ISFH).
 No

- Calculation of spectral mismatch between the reference cell and the devices under test Yes No Certified by the Institute for Solar Energy Research in Hamelin (ISFH).
6. Mask/aperture
- Size of the mask/aperture used during testing Yes No The full area of 274.4 cm² was used during testing.
- Variation of the measured short-circuit current density with the mask/aperture area Yes No The full area of 274.4 cm² was used during testing.
7. Performance certification
- Identity of the independent certification laboratory that confirmed the photovoltaic performance Yes No The photovoltaic performance was certified at the Institute for Solar Energy Research in Hamelin (ISFH) as an independent laboratory under standard test conditions.
- A copy of any certificate(s)
Provide in Supplementary Information Yes No The five certificates are presented in Figure 3b-f.
8. Statistics
- Number of solar cells tested Yes No Hundreds of cells had been tested.
- Statistical analysis of the device performance Yes No Figure 2f-i, Figure 3a and Extended Data Figure 5.
9. Long-term stability analysis
- Type of analysis, bias conditions and environmental conditions
For instance: illumination type, temperature, atmosphere humidity, encapsulation method, preconditioning temperature Yes No The long-term stability analyses are presented in Figure 4f-g, including the potential-induced degradation (PID) and light-induced degradation aging tests, and the experimental conditions are shown in the Methods section.